Journal of Magnetic Resonance 275 (2017) 137–147

Contents lists available at ScienceDirect

Journal of Magnetic Resonance

journal homepage: www.elsevier.com/locate/jmr

Comparative analysis of isotropic diffusion weighted imaging sequences

Sebastian Vellmer [a,*], Rüdiger Stirnberg [b], Daniel Edelhoff [a], Dieter Suter [a], Tony Stöcker [b,c], Ivan I. Maximov [a,*]

[a] Experimental Physics III, TU Dortmund University, Dortmund, Germany
[b] German Center for Neurodegenerative Diseases (DZNE), Bonn, Germany
[c] Department of Physics and Astronomy, University of Bonn, Bonn, Germany

ARTICLE INFO

Article history:
Received 1 August 2016
Revised 21 December 2016
Accepted 22 December 2016
Available online 30 December 2016

Keywords:
Diffusion MRI
Isotropic diffusion weightings
Microcapillary phantom
Diffusion sequences

ABSTRACT

Visualisation of living tissue structure and function is a challenging problem of modern imaging techniques. Diffusion MRI allows one to probe *in vivo* structures on a micrometer scale. However, conventional diffusion measurements are time-consuming procedures, because they require several measurements with different gradient directions. Considerable time savings are therefore possible by measurement schemes that generate an isotropic diffusion weighting in a single shot. Multiple approaches for generating isotropic diffusion weighting are known and have become very popular as useful tools in clinical research. Thus, there is a strong need for a comprehensive comparison of different isotropic weighting approaches. In the present work we introduce two new sequences based on simple (co)sine modulations and compare their performance to established *q*-space magic-angle spinning sequences and conventional DTI, using a diffusion phantom assembled from microcapillaries and *in vivo* experiments at 7 T. The advantages and disadvantages of all compared schemes are demonstrated and discussed.

1. Introduction

Investigation of living tissue functions and structures *in vivo* is a challenging problem for non-invasive imaging techniques. One of the most powerful imaging modalities is diffusion MRI (dMRI) [1], which is used extensively in research and clinical practice. dMRI utilises random Brownian motion of water molecules to visualise the underlying microstructure of biological tissue with a pulsed gradient spin echo experiment [2]. The fact that motion of water molecules within tissue compartments is restricted and hindered in contrast to free water diffusion is used to mine structural information from dMRI measurements. For instance, diffusion anisotropy originating from neuronal tissue organisation such as white matter, can be characterised by the diffusion tensor. In diffusion tensor imaging (DTI), diffusion is parametrised by a second order symmetric tensor with six degrees of freedom [3]. The consistent introduction of rotational invariants based on DTI allows one to generate a range of robust clinical biomarkers, for example, for studying tumour cellularity [4], rapid detection of strokes [5], pain research [6], chronotype research [7] and many others (see, for example, book [1] and references therein).

One of the most important biomarkers originating from DTI is the mean diffusivity (MD), which describes the averaged diffusion within one voxel. In order to determine the full diffusion tensor, at least seven measurements are required (one without diffusion weighting plus six weightings along different encoding directions). For the determination of just the MD at least three diffusion-weighted measurements with orthogonal encoding directions are required. In practice, significantly more measurements with isotropically distributed encoding directions are required [8], which leads to long dMRI acquisition times. Almost 20 years ago, it was shown that the MD metric can also be obtained directly from a single-shot measurement using isotropic diffusion weighting [9,10]. Recently, the idea of the isotropic diffusion weighting scheme found renewed interest [11–19]. In order to improve the isotropic diffusion weighting scheme Topgaard and colleagues adopted the NMR magic-angle spinning technique to the *q*-space vector [11,13,15,16]. This approach exhibits very promising results for the detection of microscopic anisotropy, orientation order [18–21] and reveals diffusion compartments [22,23]. As a result, the isotropic diffusion weighting scheme called qMAS is a fast and reliable protocol in clinical studies with an option to produce

* Corresponding authors.
E-mail addresses: vellmer@e3.physik.tu-dortmund.de (S. Vellmer), ivan@e3.physik.tu-dortmund.de (I.I. Maximov).

http://dx.doi.org/10.1016/j.jmr.2016.12.011
1090-7807/

additional scalar metrics such as microscopic fractional anisotropy, apparent kurtosis and some others [18–21].

The idea of isotropic diffusion weightings can be realised in multiple ways using the orthogonality of q-vector entries along the time axis [13]. One of the limitations of the qMAS scheme is the high demand on hardware, in particular, on the limited maximum gradient strength and the gradient slew rate [14]. We considered the limited gradient strength by correction factors and developed new pulse sequences with promising advantages. Compared to the original qMAS sequence [13], the main difference of our new sequences is that the q-vector vanishes during the refocusing pulse in the spin-echo experiment. Moreover, the $\vec{q}$-vector starts at zero, whereby we avoid the need of δ-pulses approximated by rectangular gradient functions. Thus, we employed simple (co)sine modulated functions that allowed us to introduce a straightforward implementation of the isotropical diffusion weighting gradients without needs to recall a numerical optimisation [14]. To compare the performance of these sequences, we tested them using a home-built diffusion phantom with a 14.1 T microimaging system and performed *in vivo* measurements in a 7 T MRI scanner [24].

The paper is organised as follows: the theory section describes the conditions for the development of any type of isotropic diffusion weighting sequences. The method section introduces the used experimental setups and applied post-processing algorithms. The result section presents the outcome of our tests using three typical experimental cases of free water, a microcapillary-based diffusion phantom and *in vivo* human brain measurements. We finalise the paper with a discussion, a conclusion and an outlook of our work.

2. Theory

In conventional DTI we assume that, on the scale of clinically achievable voxel dimensions, water diffusion can be described by a Gaussian propagator. In this case, the diffusion signal attenuation is modelled by the second order symmetric diffusion tensor $\mathbf{D}$ [3]:

$$S = S_0 \exp\left(-b\vec{g}^T\mathbf{D}\vec{g}\right), \tag{1}$$

where S_0 is the signal without the applied diffusion encoding gradients, b is the diffusion weighting factor (the so-called b-value) and the direction of the applied diffusion gradients is determined by the unit vector $\vec{g} = (g_x, g_y, g_z)$. Measurements along at least 6 non-coplanar diffusion encoding directions allow us to reconstruct the full diffusion tensor

$$\mathbf{D} = \begin{pmatrix} D_{xx} & D_{xy} & D_{xz} \\ D_{yx} & D_{yy} & D_{yz} \\ D_{zx} & D_{zy} & D_{zz} \end{pmatrix}. \tag{2}$$

This tensor can be used as the source for several derived scalar metrics, for example, the mean diffusivity

$$\mathrm{MD} = \frac{1}{3}\mathrm{Tr}(\mathbf{D}). \tag{3}$$

For more metrics see Ref. [25]. In the case of time-varying gradient fields $\vec{G}(t)$ Eq. (1) can be generalised as follows [25,26]:

$$S = S_0 \exp\left(-\int_0^{t_e} \vec{q}(t)^T\mathbf{D}(t)\vec{q}(t)dt\right), \tag{4}$$

where the dephasing vector $\vec{q}(t)$ is

$$\vec{q}(t) = \gamma\int_0^t \vec{G}(\tau)f(\tau)d\tau, \tag{5}$$

γ is the gyromagnetic ratio and t_e is the echo time. The factor $f(\tau)$ considers that the magnetisation can be flipped by a π-pulse so it is 1 in the beginning of the sequence and changes its sign when a π-pulse is applied. The dephasing vector $\vec{q}(t)$ must satisfy the condition $\vec{q}(0) = \vec{q}(t_e) = 0$. Note, that in general the diffusion coefficients $D_{ij}(t)$ in Eq. (4) are time-dependent [27]. Thus, in the case of isotropic weighting sequence the estimated MD represents a weighted average over the time. However, using the Gaussian approximation we assume that the dependence of diffusion coefficients on time can be omitted.

According to Eq. (3), isotropic diffusion weighting is obtained when the weight of the diagonal elements of $\mathbf{D}$ is equal and the weight of the off-diagonal elements vanishes [9,10,28]. This condition is achieved by an orthogonalisation of the dephasing vector $q(t)$ entries

$$\int_0^{t_e} q_i(t)q_j(t)\mathrm{d}t = \frac{b}{3}\delta_{ij}, \quad i,j = x,y,z, \tag{6}$$

where $\delta_{ii} = 1$ is the Kronecker delta-function. The b-values are defined by the relation in Eq. (6) and equal to $b = \sum_i \int_0^{t_e} q_i(t)q_i(t)dt$. The signal attenuation in case of isotropic diffusion weighting is then

$$S = S_0 \exp\left(-b \cdot \mathrm{MD}\right). \tag{7}$$

The condition (6) can be fulfilled using different types of time-dependent functions $\vec{G}(t)$, for example simple rectangular pulses [9,10], orthogonal functions such as bipolar gradient pulse pairs [15], or general functions derived from numerical optimisation [14]. In the next section we describe a few approaches to isotropic diffusion weighting using functions $\vec{G}(t)$ that fulfil equation (6).

3. Isotropic diffusion weighting sequences

For all isotropic diffusion weighting sequences the classical Stejskal-Tanner spin-echo (SE) sequence was chosen as a basis [2]. Initially, the magnetisation is flipped into the xy-plane by a 90°-pulse. Following a train of diffusion encoding gradients the magnetisation is refocused by a 180°-pulse that generates a spin-echo at time t_e. The diffusion gradients encode trajectory information of spin-carrying molecules in such a manner that an attenuation of the magnetisation due to self-diffusion would be observed. The time between the two rectangular gradient pulses of the Stejskal-Tanner sequence is the diffusion time Δ, measured from the beginning of the first one to the beginning of the second one. The readout section of the sequence depends on the application. In the microimaging system we used sequential line readouts, whereas *in vivo* experiments demanded fast echo-planar imaging (EPI) acquisitions.

3.1. q-Space Magic-Angle Spinning (qMAS)

The q-space trajectory of the original qMAS sequence [13,11] starts with a straight line along the positive z-axis employing a rectangular gradient pulse of length δ, as shown in Fig. 1a. Subsequently, the time-dependent diffusion gradients $\vec{G}(t)$ perform the magic-angle spinning of $\vec{q}(t)$. During the refocusing RF pulse, the rotation of the $\vec{q}$-vector is interrupted for a time t_{180} (see Fig. 1a). Exact duration of the refocusing pulse t_{180} depends on MRI hardware and modality (imaging or spectroscopy). It can be up to several 10 ms. As a result, the off-diagonal elements of the diffusion tensor $\mathbf{D}$ contribute to the signal attenuation for this sequence. Moreover, the diagonal elements of the diffusion tensor obtain different weightings for finite δ and t_{180}, i.e. affecting the condition in Eq. (6). The second deviation from the ideal behaviour can be corrected by scaling the gradient amplitudes G_i with a factor α_i for each direction i, but not the first one.

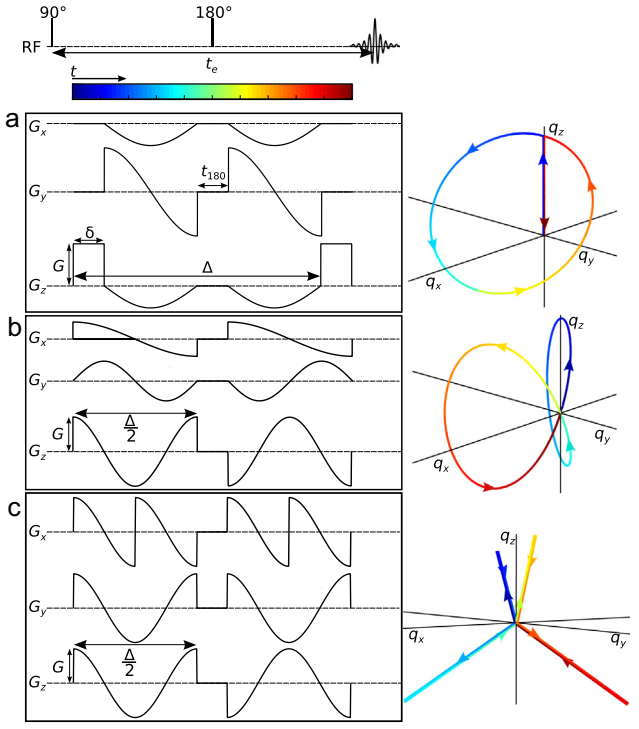

Fig. 1. Schemes of the isotropic diffusion weighting sequences (left) and the corresponding $\vec{q}$-trajectories (right). RF pulses and colour-encoded time scale are presented on the top. (a) qMASmod, (b) FAMED, (c) FAMEDcos. (For interpretation of the references to colour in this figure legend, the reader is referred to the web version of this article.)

In order to adjust the weight of the diagonal elements and thereby generate a b-value in accordance with the Stejskal-Tanner sequence $b_{\text{qMAS}} = b_{\text{ST}} = G^2\gamma^2\delta^2(\Delta - \delta/3)$ we use the scaling factors

$$\alpha_i = \sqrt{\frac{b_{\text{ST}}}{3\int_0^{t_e} q_i^2(t)dt}}. \tag{8}$$

For the qMAS sequence, these factors become

$$\vec{\alpha} = \left(\sqrt{\frac{\Delta - \frac{1}{3}\delta}{\Delta + \frac{5}{3}t_{180} - \delta}}, \sqrt{\frac{\Delta - \frac{1}{3}\delta}{\Delta - t_{180} - \delta}}, \sqrt{\frac{\Delta - \frac{1}{3}\delta}{\Delta - \frac{2}{3}t_{180} + \delta}}\right). \tag{9}$$

For example, for *in vivo* measurements using the SE EPI experiment a typical parameter set is $t_{180} = 16$ ms, $\Delta = 83.2$ ms and $\delta = 12.8$ ms so we obtain the scaling factor as $\vec{\alpha} = (0.90, 1.20, 0.96)$. We refer to the qMAS sequence modified by our corrections to qMASmod.

As noted above, due to non-zero $\vec{q}$-vector during the refocusing pulse the qMAS sequence always weighs the off-diagonal tensor elements. In the used example we obtain the off-diagonal weighting

$$\begin{aligned}\int_{\frac{\Delta-\delta-t_{180}}{2}}^{\frac{\Delta-\delta+t_{180}}{2}} \sum_{i\neq j} q_i(t)D_{ij}q_j(t)dt &= 2t_{180}D_{xz}q_x\left(\frac{\Delta-\delta}{2}\right)q_z\left(\frac{\Delta-\delta}{2}\right)\\ &= -\frac{8\sqrt{2}}{9}t_{180}G^2\alpha_x\alpha_z\gamma^2\delta^2D_{xz}\\ &\approx 0.22bD_{xz}.\end{aligned} \tag{10}$$

3.2. FAst MEan Diffusion (FAMED)

To avoid the contribution of off-diagonal elements, we propose an alternative set of the diffusion encoding gradient functions. The condition in Eq. (6) of the orthogonality for $\vec{q}(t_{180})$-components should be extended by an additional condition $\vec{q}(t) = 0$ during the delay time t_{180} applied for the refocusing pulse. We define the time-dependence as

$$\vec{G}(t) = G\begin{cases}\begin{pmatrix}\frac{1}{2}\cos\left(\frac{2\pi}{\Delta}t\right)\\ \frac{1}{\sqrt{3}}\sin\left(\frac{4\pi}{\Delta}t\right)\\ \cos\left(\frac{4\pi}{\Delta}t\right)\end{pmatrix}, & \text{if } 0 < t \leqslant \frac{\Delta}{2}.\\ \vec{0}, & \text{if } \frac{\Delta}{2} < t \leqslant \frac{\Delta}{2} + t_{180}.\\ -\begin{pmatrix}\frac{1}{2}\cos\left(\frac{2\pi}{\Delta}(t-t_{180})\right)\\ \frac{1}{\sqrt{3}}\sin\left(\frac{4\pi}{\Delta}(t-t_{180})\right)\\ \cos\left(\frac{4\pi}{\Delta}(t-t_{180})\right)\end{pmatrix}, & \begin{array}{l}\text{if } \frac{\Delta}{2} + t_{180} < t.\\ t \leqslant \Delta + t_{180}.\end{array}\end{cases} \tag{11}$$

Fig. 1b shows a schematic representation of this sequence. The corresponding b-value is

$$b_{\text{FAMED}} = 3\int_0^{t_e} q_i(t)q_i(t)dt = G^2\gamma^2\frac{3\Delta^3}{32\pi^2}. \tag{12}$$

The isotropic weighting of the FAMED sequence is thus independent of the off-diagonal terms generated during the time t_{180}.

We have to emphasise here, that while this scheme generates an isotropic diffusion weighting for a time-independent diffusion tensor, this is no longer the case for restricted diffusion or compartmentalised systems, where the diffusion tensor becomes time-dependent. In the qMAS sequence, as well as in the FAMED sequence (see Figs. 1a and b) the $\vec{q}(t)$-vector components have different numbers of zero-crossings and therefore different times between them. As a result, different diffusion weightings are generated if the time dependence of diffusion coefficients is not negligible.

3.3. FAMED-cosine (FAMEDcos)

This anisotropic contribution from restricted diffusion can be eliminated by modulating all three components of the gradient with the same frequency. A set of orthogonal functions with equal frequencies is

$$\vec{G}(t) = G\begin{cases}\begin{pmatrix}\cos\left(\frac{4\pi}{\Delta}t + \phi\right)\\ \cos\left(\frac{4\pi}{\Delta}t\right)\\ \cos\left(\frac{4\pi}{\Delta}t + \theta\right)\end{pmatrix}, & \text{if } 0 < t \leqslant \frac{\Delta}{2}.\\ \vec{0}, & \text{if } \frac{\Delta}{2} < t \leqslant \frac{\Delta}{2} + t_{180}.\\ -\begin{pmatrix}\cos\left(\frac{4\pi}{\Delta}(t-t_{180}+\phi)\right)\\ \cos\left(\frac{4\pi}{\Delta}(t-t_{180})\right)\\ \cos\left(\frac{4\pi}{\Delta}(t-t_{180}+\theta)\right)\end{pmatrix}, & \begin{array}{l}\text{if } \frac{\Delta}{2} + t_{180} < t.\\ t \leqslant \Delta + t_{180}.\end{array}\end{cases} \tag{13}$$

$$\phi = \begin{cases}\pi & \text{if } \leqslant \frac{\Delta}{4} < t \leqslant \frac{\Delta}{2}.\\ \pi & \text{if } \leqslant \frac{3\Delta}{4} + t_{180} < t \leqslant \Delta + t_{180}.\\ 0 & \text{else}\end{cases}$$

$$\theta = \begin{cases}\pi & \text{if } \leqslant \frac{\Delta}{2} + t_{180} < t \leqslant \Delta + t_{180}.\\ 0 & \text{else}\end{cases}$$

Fig. 1c shows a schematic representation of this sequence. Its b-value is

$$b_{\text{FAMEDcos}} = 3\int_0^{t_e} q_i(t)q_i(t)dt = G^2\gamma^2\frac{3\Delta^3}{32\pi^2}. \tag{14}$$

Notably, the q-trajectory of FAMEDcos is composed of straight lines from the origin to vertices of a tetrahedron and back to the origin. Such a trajectory shape could be replicated using four pairs of δ-pulses. A powerful advantage of FAMEDcos scheme in contrast to other isotropic sequences is a possible generalisation in terms of isotropically oscillating gradients, when the frequency along all

axes is the same. This generalisation allows one to determine the time dependence of the MD for short diffusion times by varying the frequency.

4. Methods

We compared isotropic weighting schemes on three samples: a phantom with free water, an anisotropic microcapillary phantom and *in vivo* on a human brain. All phantom measurements were performed using our wide-bore 14.1 T microimaging Varian system. The system is equipped with gradient coils providing amplitudes up to 3 T/m in *z*-direction and 2 T/m in *x*- and *y*-direction. The temperature inside of the system was 15.6 °C.

4.1. Free water

As a simple and robust test we measured free water diffusion in a 5 mm NMR tube filled with distilled water. We compared the results of six different sequences without imaging encoding: the conventional Stejskal-Tanner sequence, Mori's version of the isotropic diffusion weighting (Pattern I in Ref. [9]), FAMED, FAMEDcos, original qMAS, and qMAS with corrected weights (qMASmod). The MDs were determined by linear fitting of the logarithm of the measured signals versus *b*-values.

4.2. Microcapillary phantom

To verify the expected differences between the isotropic diffusion weighting schemes, we built a phantom with well-known anisotropic compartments that limit the water diffusion. This phantom consists of a bundle of fused silica microcapillaries (Polymicro Technologies™ Molex) of different inner diameters (5 μm, 10 μm, and 20 μm), chosen to be comparable to the anisotropy of typical neuronal tissue, such as white matter in the human brain (see Fig. 2).

Table 1 summarises the relevant experimental parameters used in the measurements. Because of the symmetry of the sample along the *z*-axis we used a voxel size of $4 \times 4 \times 10^3$ μm^3 to resolve the signal within the capillaries and improve the signal-to-noise ratio (SNR). We compared four different sequences: conventional DTI with 6 directions $[(1,1,0),(1,-1,0),(1,0,1),(1,0,-1),(0,1,1),(0,1,-1)]$, qMASmod, FAMED, and FAMEDcos. In order to calculate the MD for the three types of compartments, namely, extra-capillary water, 20 μm and the 10 μm microcapillaries, we manually defined a set of regions of interest (ROI) (see Fig. 4c). For the intra-capillary data we first integrated the signal of one microcapillary in order to calculate the MD. Subsequently, we averaged the MD values over all capillaries. For the calculation of the extra-capillary MD we averaged voxelwise over three large compartments.

In order to estimate time dependent variations of MD values for the FAMED, FAMEDcos, and qMASmod approaches we also performed measurements with varying diffusion times Δ ranging from 0.04 to 0.1 s in steps of 0.01 s. As a sample with complex substructure mimicking neural tissue we measured diffusion in the phantom without applying imaging gradients. A set of *b*-values equal to $(0.3, 0.6, 0.9) \cdot 10^9$ s/m^2 was used. For the qMASmod sequence we used $\delta = 1$ ms and $t_{180} = 1.8$ ms.

4.3. In vivo measurements

In vivo data were acquired on a Siemens whole body 7 T MAGNETOM scanner (Siemens Medical Systems, Erlangen, Germany) equipped with a 70 mT/m gradient system with a maximum slew rate of 200 T/m/s and a 32 channel head coil. We measured one 23 years old healthy volunteer who gave written informed consent prior to participation. The volunteer had no self-reported history of any psychiatric or neurological diseases and did not suffer from any brain injuries. The study was approved by the local ethical committee.

We implemented four diffusion enconding schemes: Stejskal-Tanner, qMASmod, FAMED, and FAMEDcos combining them with conventional SE EPI. Table 2 summarises the imaging parameters for three cases: *in vivo* isotropic weighting measurements (Protocol 1), different diffusion times Δ (Protocol 2), and rotational invariance of the proposed schemes (Protocol 3). For DTI, we used 30 isotropic diffusion directions defined by a deterministic DIrection SCheme Obtained By ALigning points on Latitudes (DISCOBALL) [29].

Image post-processing was done as follows: first the *in vivo* data were corrected for susceptibility and eddy-current induced distortions and subject motion using the *eddy* utility from the FSL package [30]. The appropriate *b*-matrix rotation for DTI was performed using Matlab (Mathworks, Natick, USA) [31]. In order to improve SNR noise was corrected by assuming the non-central χ^2 distribution [32] due to employed parallel imaging (GRAPPA acceleration factor 2). The Gibbs ringing effect close to contrast edges such as ventricles was suppressed by Gaussian smoothing with a kernel of $1.5 \times 1.5 \times 1.5$ mm^3 [33]. The MD metric for DTI was estimated using ExploreDTI and a linear weighted least squares method [34]. In the case of qMASmod, FAMED, and FAMEDcos we evaluated the MD values using Matlab and a linear least squares method.

In order to quantify the differences between the isotropic diffusion weighting schemes we used three ROIs in addition to a whole brain mask. The latter was defined using the Brain Extraction Tool (BET) from the FSL package [35]. The corticospinal tract (CST), and a part of the corpus callosum, namely the splenium, were localised by employing streamline tractography on the DTI data using ExploreDTI. The CST contains regions with crossing fibres, e.g. in the connection to the corpus callosum, while the splenium has a very coherent axon bundle. These two types of tracts allowed us to check for a possible bias in the metric validation. A third ROI was defined by the volume of the lateral ventricles, which contain cerebrospinal fluid (CSF). Pearson correlation coefficients were calculated according to the pair comparisons DTI vs qMASmod, DTI vs FAMED, and qMASmod vs FAMED sequences.

We assessed the time dependence of the MD metrics for FAMED, and FAMEDcos schemes *in vivo* by varying the diffusion time Δ from 76 up to 92 ms, and qMASmod with Δ from 98.6 up to 99.9 ms with diffusion weighting fixed to $b = 5 \cdot 10^8$ s/m^2 (see Table 2: Protocol 2).

In order to prove a rotational invariance of the isotropic diffusion weighting schemes we performed systematic sequence rotation for qMAS, qMASmod, FAMED and FAMEDcos around the *y*-axes covering 360°. The rotation step angle was $\theta = 30^\circ$. We used *b*-values equal to 10^9 s/m^2 for qMAS, qMASmod, and FAMED and $7 \cdot 10^8$ s/m^2 for FAMEDcos (see Table 2: Protocol 3). The *b*-value for FAMEDcos was reduced due to integrated safety test to prevent peripheral nerve stimulation. To estimate the influence of rotations on the MD metrics we required well defined, coherent directions of diffusion. Therefore we defined a fourth ROI according to FA > 0.2 and $\alpha < \pi/6$, where α denotes the angle between the main eigenvector and the *x* or *z*-axis.

5. Results

5.1. Phantom measurements

Fig. 3 shows the signal attenuation of free water for all sequences with *b*-values up to 10^9 s/m^2. Table 3 lists the

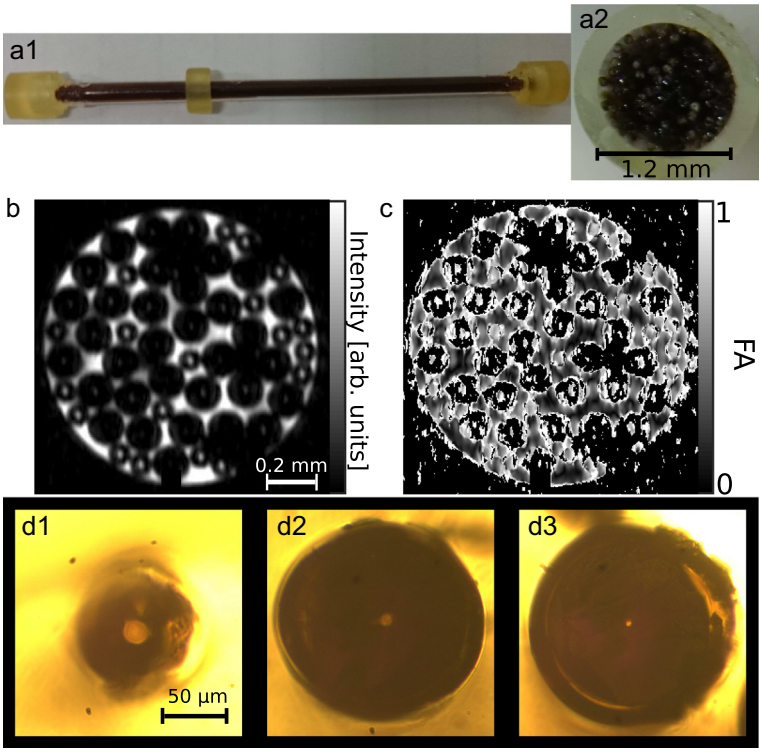

Fig. 2. Home-built anisotropic diffusion phantom. (a) Images of the used microcapillary phantom (a1) used phantom, and (a2) cross section of the phantom before closing. (b) SE image of the water filled phantom. (c) Fractional anisotropy of the phantom estimated from DTI measurements (see text). (d) Optical microscopic images of single microcapillaries with inner diameters of (d1) 20 µm, (d2) 10 µm, (d3) 5 µm.

Table 1
Experimental parameters for the diffusion phantom measurements. Maximal gradient strength (GS) and maximal gradient vector length (MVL).

Sequence	Δ [ms]	δ [ms]	t_{180} [ms]	t_e [ms]	TR [s]	b [s/m^2]	GS [mT/m]	MVL [mT/m]
DTI	40	1	1.8	50	10	10^9	594	594
qMASmod	40	1	1.8	50	10	10^9	594	594
FAMED	40	-	1.8	50	10	10^9	152	170
FAMEDcos	40	-	1.8	50	10	10^9	152	263

Table 2
Imaging parameters for *in vivo* measurements (Protocol 1), for different diffusion times (Protocol 2), and for gradient rotations (Protocol 3). Number of averages (N_a) of different diffusion weighted images, acquisition time (TA), and maximal gradient strength (GS), voxel size in all measurements was $1.8 \times 1.8 \times 1.8$ mm^3. Value intervals are presented as [min:step:max].

Sequence	t_e [ms]	TR [s]	Δ [ms]	δ [ms]	b [s/m^2]	N_a	TA [min]	GS [mT/m]
Protocol 1								
DTI	130	10	65	50	$1 \cdot 10^9$	1	5:20	11
qMASmod	130	10	99	16	$1 \cdot 10^9$	9	1:44	34
FAMED	130	10	100	–	$1 \cdot 10^9$	9	1:44	38
Protocol 2								
qMASmod	120	10	[98.6:0.3:99.9]	[6.1:0.3:7.4]	$5 \cdot 10^8$	4	1:10	27
FAMED	120	10	[76:4:92]	–	$5 \cdot 10^8$	4	1:10	41
FAMEDcos	120	10	[76:4:92]	–	$5 \cdot 10^8$	4	1:10	41
Protocol 3								
qMAS	127	10	97	16	$1 \cdot 10^9$	2	4:30	30
qMASmod	127	10	97	16	$1 \cdot 10^9$	2	4:30	34
FAMED	130	10	100	–	$1 \cdot 10^9$	2	4:30	38
FAMEDcos	120	10	92	–	$7 \cdot 10^8$	2	4:30	36

resulting MD values and the relevant experimental parameters. The obtained values are close to the literature value of $1.81 \cdot 10^{-9}$ m^2/s, interpolated from the experimental data in Ref. [36].

Fig. 4 presents the mean diffusivity maps of the anisotropic microcapillary phantom and the resulting averaged values for three defined regions. The MD results for varying diffusion times with qMASmod, FAMED and FAMEDcos are presented in Fig. 5.

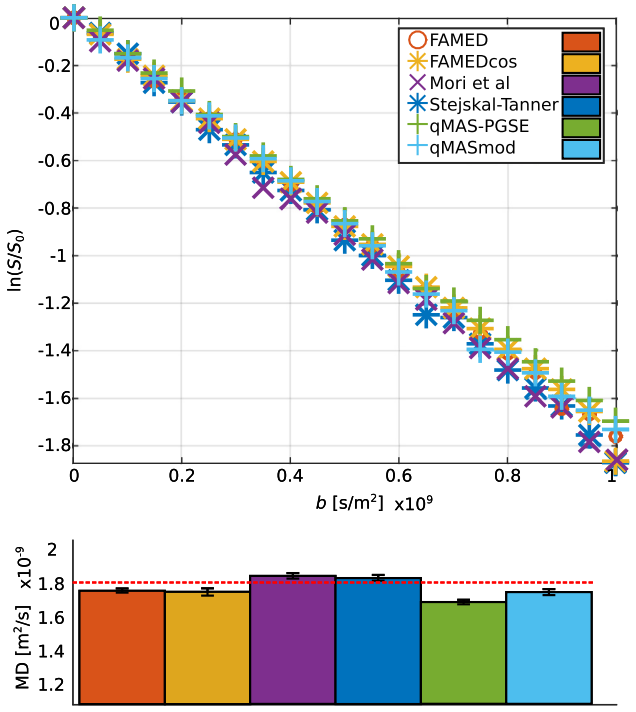

Fig. 3. Top: Attenuation of the free water signal for different diffusion encoding sequences measured at 15.6 °C. Bottom: Mean diffusivities determined from a linear least squares fit of the data. The literature value of free water diffusion $1.81 \cdot 10^{-9}$ m^2/s [36] is presented as a dashed red line. The error bars represent the 95% interval of confidence. (For interpretation of the references to colour in this figure legend, the reader is referred to the web version of this article.)

Table 3
MD of free water from the data of Fig. 3, with the relevant experimental parameters (see Fig. 1 for definitions). Delay time t_{180} was 2.64 ms, echo time t_e was 55 ms, repetition time (TR) was 10 s; Dev – deviation from the literature value $1.81 \cdot 10^{-9}$ m^2/s [36].

Sequences	MD [10^{-9} m^2/s]	Δ [ms]	δ [ms]	Dev [%]
FAMED	1.77 ± 0.03	50	–	−2.2
FAMEDcos	1.76 ± 0.05	50	–	−2.8
Stejskal-Tanner	1.84 ± 0.04	50	1	1.7
Mori and Van Zijl [9]	1.85 ± 0.04	15	1	2.2
qMAS [28]	1.70 ± 0.03	50	1	−6.1
qMASmod	1.76 ± 0.04	50	1	−2.7

5.2. In vivo measurements

Fig. 6 shows histograms of the whole brain MD distribution as well as for three specific ROIs.

Fig. 7 shows that all correlations between MD estimates obtained from different measurements (DTI, qMASmod and FAMED) are quite high.

Averaged MD values for varying diffusion times obtained from the same ROIs as in Fig. 6 are presented in Fig. 8.

Fig. 9 shows corresponding MD values obtained from coherent fibre bundles which are parallel to the *x*-axis and the *z*-axis during the rotation of the diffusion weighting scheme around the *y*-axis.

6. Discussion

In the present work we performed a comparison of isotropic diffusion weighting schemes to the conventional Stejskal-Tanner DTI sequence. The novel FAMED and FAMEDcos sequences allowed us to avoid problems associated with qMAS and qMASmod such as induced non-isotropic weightings during the RF refocusing pulse period in *q*-space. *In vivo* applications of the FAMED and FAMEDcos exhibited excellent agreement with MD from conventional DTI at ultra-high field MRI and allowed us to obtain MD metrics in a single-shot acquisition without additional needs of numerical optimisation.

In the free water experiment we applied different pulse sequences possessing isotropic diffusion weighting in order to provide a highly robust test. Obtained results from all sequences are in excellent mutual agreement and with the literature value [36]. The evaluated MD values are slightly higher for sequences that use rectangular gradient pulses, namely, conventional Stejskal-Tanner [2] and Mori's sequence [9]. The sequences using harmonic gradient shapes, FAMED, FAMEDcos and qMASmod yield very closely agreeing MD metrics. Interestingly, we observed a significantly lower value of the diffusion coefficient in the case of the original qMAS sequence than in the other measurements. Due to the neglect of the finite rectangular pulses and the time t_{180} the used *b*-values are lower than the real diffusion weighting which results in a lower MD in the case of original qMAS. A small deviation of the MD metrics obtained by FAMED, FAMEDcos and qMASmod in contrast to the Stejskal-Tanner sequence can be explained by the finite precision of the discretised sine and cosine functions implemented on the spectrometer. However, we expected to observe a good agreement for all isotropic weighting schemes due to the validity of the Gaussian propagator model for free water.

The home-built anisotropic diffusion phantom allowed us to test the behaviour of the isotropic diffusion weighting sequences in the presence of strong anisotropy. A bundle of microcapillaries of different inner diameters was aligned along the external magnetic field to minimise the susceptibility distortions. Microscopic in-plane imaging with a voxel size of 4×4 µm^2 allowed us to perform manual segmentation of different regions of the phantom. However, the resulting images still suffer from motion artefacts generated by the strong switching gradients (see Fig. 4). The signal decay within the extra-capillary space agrees well with Gaussian diffusion of free water. Consequently, the MD values obtained in the extra-capillary space confirm the results from the free water experiment (see Fig. 4).

The diffusion microscopy images suffer from multiple distortions, such as partial volume effects, motion artefacts, and low SNR. For example, the diffusion signal inside of capillaries with 5 µm diameter are too small for analysis and have therefore been ignored in the present work. Nevertheless, all isotropic weighting schemes yield a high contrast for restricted vs extra-capillary water. In this context small sequence imperfections play an important role: the number of zero-crossings of the $\vec{q}$-vector entries, rescaling of gradient functions, and the relatively coarse gradient discretisation limit the accuracy of the diffusion measurements. One of the assumptions for application of the isotropic weighted schemes is that the time dependence of the diffusion coefficients is negligible. In order to validate a relevance of this assumption we assessed MD values for varying diffusion times (see Fig. 5). As we already mentioned, the MD values, in fact, represent time averaged metrics. The sampled diffusion time range $\Delta \subset [0.04, 0.1] \cdot 10^{-3}$ s and characteristic length of $l \approx 10^{-4}$ m correspond to a short diffusion limit, the so-called Mitra limit [27]. One can see that qMASmod exhibits very strong variability at short diffusion times compared to FAMED and FAMEDcos. In turn, the time dependence becomes less pronounced for $\Delta > 0.08$ s, in particular, in the case of FAMEDcos.

In vivo measurements demonstrated a practical clinical application of the isotropic diffusion weighting approach. The DTI measurements based on Stejskal-Tanner diffusion weighting along a

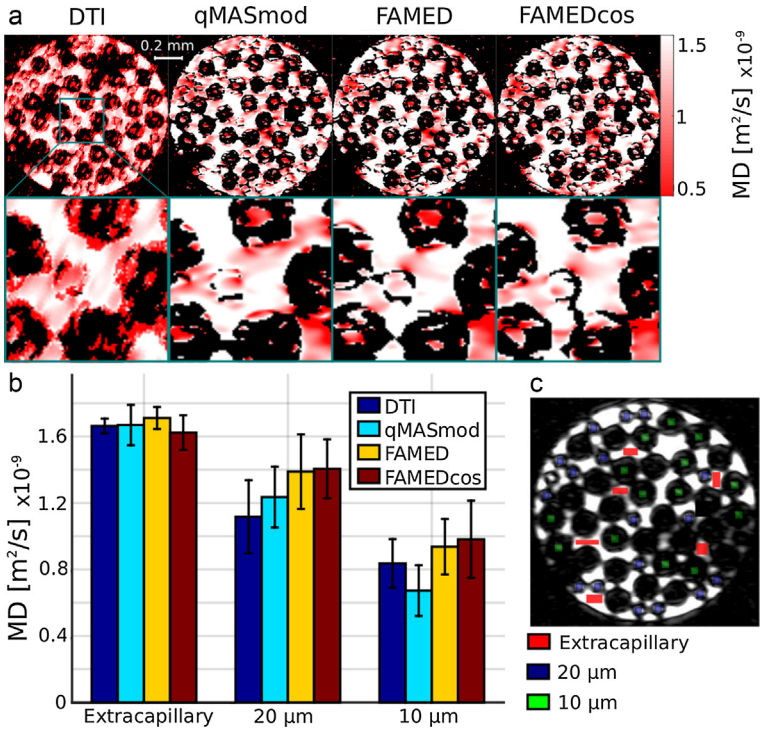

Fig. 4. Measurements on the home-built anisotropic phantom. (a) MD maps for the four sequences, (b) average over ROIs, (c) used masks for ROIs. We used $4 \times 4 \times 10^3$ µm^3 voxel size. The averaged diffusion coefficients for the three ROIs are presented as bar graphs for the different diffusion schemes. The drawn error bars represent the standard deviation from the mean value.

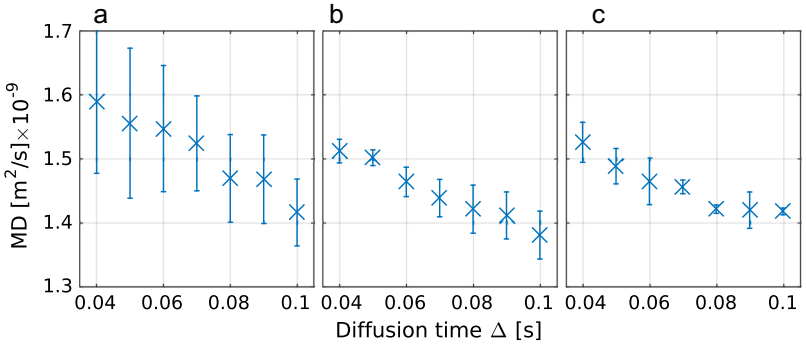

Fig. 5. Estimated MD of the anisotropic phantom for different diffusion times Δ for (a) qMASmod, (b) FAMED and (c) FAMEDcos approaches. The MDs were estimated by linear fitting of the signal attenuation with the *b*-values 0.3, 0.6 and $0.9 \cdot 10^9$ s/m^2. The error bars represent the 95% interval of confidence.

large number of encoding directions can be considered as the "gold standard" in the sense of quantitative metrics and contrast quality. In order to reduce a possible bias in the metric assessment due to the post-processing steps [37] and algorithmic variations [38] we analysed the data in a conventional way using standard tools from the FSL package [30], and applying weighted linear and linear least squares algorithms. The analysis results show that, the agreement between DTI, qMASmod and FAMED is very high for all regions of interest, including the whole brain mask (see Figs. 6 and 7). In order to validate the MD metrics in typical white matter regions we reconstructed two characteristic fibre tracts using a DTI-based streamline algorithm: the splenium, which is a part of the corpus callosum, and the corticospinal tract. All data including fibre tract segmentation exhibited very high correlation coefficients for the MD values. The averaged MD values for the CST (DTI: 0.77 ± 0.30; qMASmod: 0.95 ± 0.34; FAMED: 0.82 ± 0.22) m^2/s and the splenium (DTI: 0.95 ± 0.45; qMASmod: 1.05 ± 0.42; FAMED: 0.89 ± 0.32) m^2/s are in the range of typical MD values from lifespan studies [39,40] (0.80 m^2/s and 0.80 m^2/s, respectively). Surprisingly, the FAMED metrics exhibited lower standard deviations over the tracts and closer mean metrics. The MD metrics from DTI exhibit an increased variability, possibly due to outliers [41], increased motion sensitivity because of a longer acquisition time and post-processing steps [38].

It is very interesting, that for the *in vivo* case the time dependence of the diffusion coefficient measurements is almost negligible (see Fig. 8.) Moreover, in highly anisotropic regions such as CST or splenium all schemes exhibited similar results. A principle difference between the approaches could be revealed by spatial rotations of the gradients around the *y*-axis (see Fig. 9). In this case both qMAS and qMASmod failed to prove their rotational invariance in contrast to the FAMED and FAMEDcos. A remark-

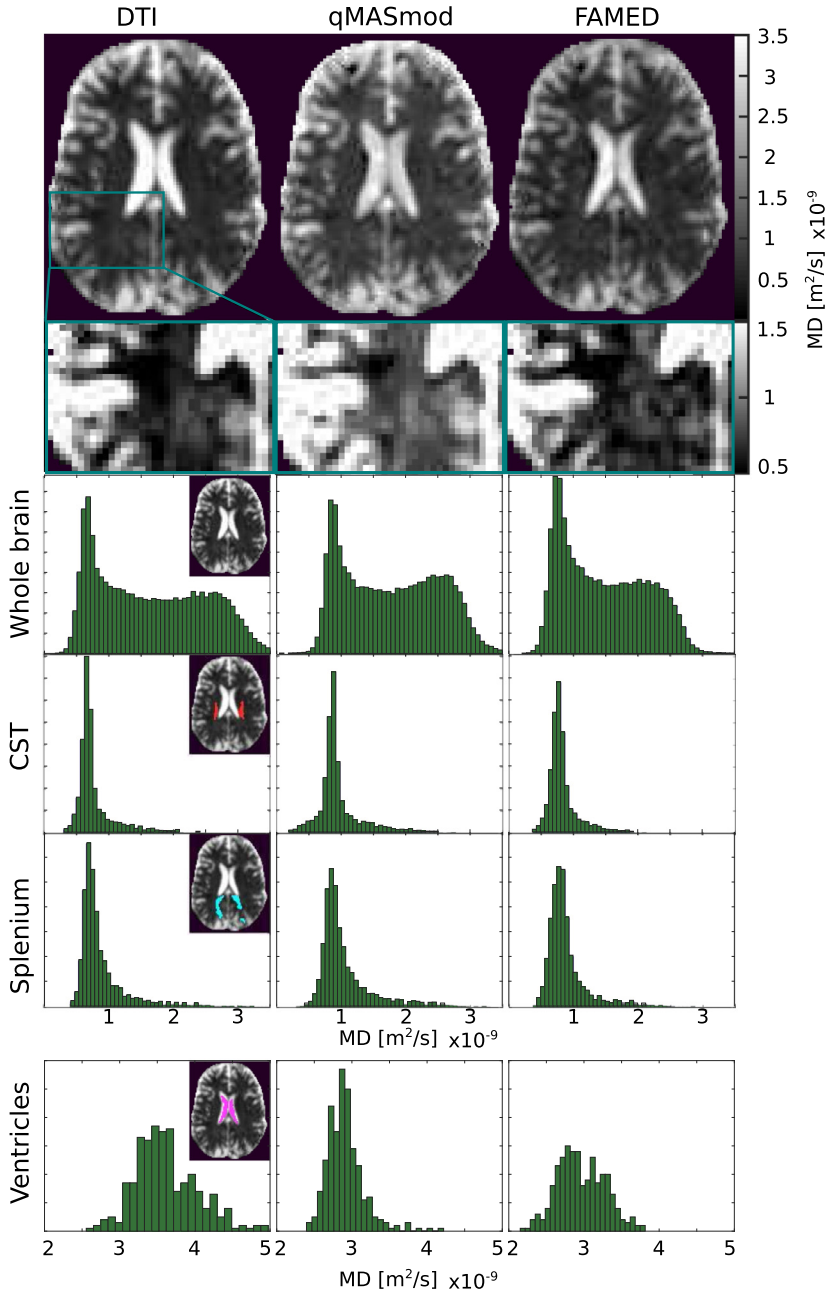

Fig. 6. Estimated MD metrics for *in vivo* measurements. Zoomed images using narrower contrast scaling emphasise a contrast difference between the isotropic diffusion weighting imaging schemes. A qualitative histogram comparison is performed using four brain regions: whole brain volume, corticospinal tract (CST), splenium tract, and ventricles.

able difference between FAMED and FAMEDcos was observed when the main eigenvector of the diffusion tensor was parallel either to the *x*-axis or to the *z*-axis. In the case when the main eigenvectors are parallel to *x*-axis, FAMED and FAMEDcos exhibited significantly different MD metrics. On the other hand, main eigenvectors parallel to the *z*-axis did not reveal such difference. In both cases the variation of the results is higher for FAMEDcos. The higher variability of the MD metrics can be explained by stronger demands on the gradient system.

In summary, we have demonstrated that the novel isotropic diffusion weighting sequences FAMED, FAMEDcos and qMASmod, are very powerful approaches with a potentially great impact for clinical applications. Therefore isotropic diffusion weighted imaging may allow us to rephrase a question formulated in Ref. [42]: "six is enough?" to the answer: "single-shot is enough".

7. Conclusion

We have shown that isotropic diffusion weighting schemes such as FAMED, FAMEDcos or qMASmod satisfy high imaging standards. The efficiency of single-shot isotropic diffusion weighting is particularly promising where measurement time constraints or motion sensitivity would otherwise limit, or even prevent application of conventional DTI, for example, in the case of strokes [5], hyperpolarisation experiments [43,44], fast-going processes [45] or high-resolution imaging. We hope that in the future these

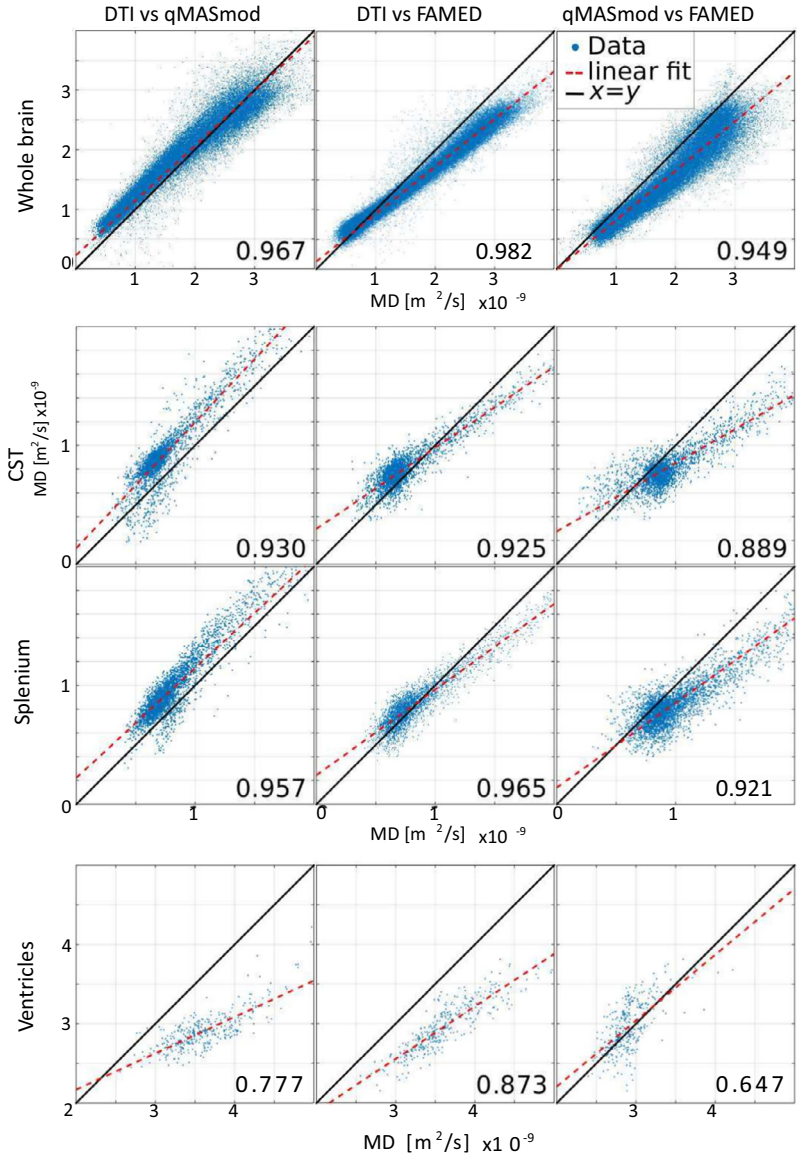

Fig. 7. Scatter plots and Pearson correlation of the MD metrics estimated with different diffusion weighting sequences *in vivo*. The regions correspond to the same ROIs as in Fig. 6.

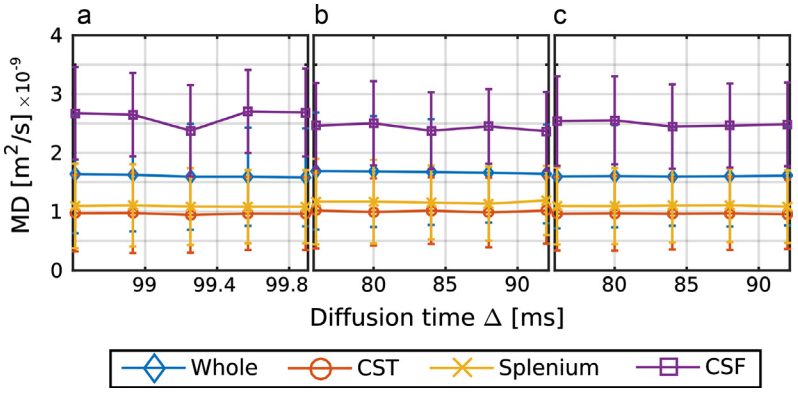

Fig. 8. Time dependence of MD metrics averaged over the same ROIs as in Fig. 6. Schemes are (a) qMASmod, (b) FAMED and (c) FAMEDcos.

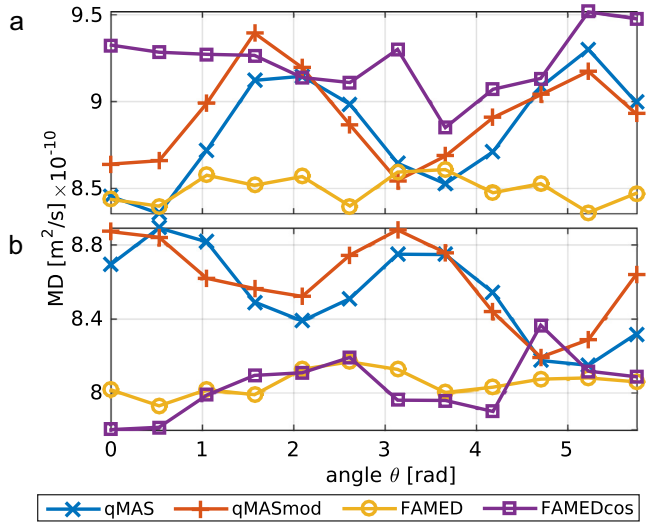

Fig. 9. Averaged MD as a function of gradient rotation around the *y*-axis for qMAS, qMASmod, FAMED and FAMEDcos. We averaged MD values over the ROI that is defined in the text. (a) Main eigenvector is parallel to the *x*-axis and (b) the main eigenvector is parallel to the *z*-axis.

approaches will find their place as a robust and reliable diagnostic method.

8. Outlook

Isotropic diffusion weighted imaging is easily adopted for research and clinical applications, not only on modern imaging facilities such as 7 T human MRI scanners, but also on widely accessible 3 T and 1.5 T systems. Besides brain imaging, abdominal diffusion imaging, which suffers from pronounced shot-to-shot motion artefacts, may be another promising application. In the future we expect to demonstrate an advantage of the isotropic diffusion weighting for biophysical modelling such as kurtosis imaging [19,46] or bi-compartment models [22] and the time-dependence of the diffusion [47] including isotropic oscillating gradients [48] based on FAMEDcos scheme.

Acknowledgement

The work was financially supported by the DFG Grant SU 192/32-1. The authors thank Dr. Daniel Brenner for providing a flexible interface to implementing harmonic gradient waveforms on the 7T MRI scanner as well as the ITMC of TU Dortmund University for an accessible computational facility at the LiDo cluster.

References

[1] H. Jonhansen-Berg, T. Behrens, Diffusion MRI: From Quantitative Measurement to In Vivo Neuroanatomy, Elsevier, 2013.
[2] E.O. Stejskal, J.E. Tanner, Spin diffusion measurements: spin echoes in the presence of a time-dependent field gradient, J. Chem. Phys. 42 (1) (1965) 288–292.
[3] P.J. Basser, J. Mattiello, D. LeBihan, MR diffusion tensor spectroscopy and imaging, Biophys. J. 66 (1) (1994) 259.
[4] L. Chen, M. Liu, J. Bao, Y. Xia, J. Zhang, L. Zhang, X. Huang, J. Wang, The correlation between apparent diffusion coefficient and tumor cellularity in patients: a meta-analysis, PloS One 8 (11) (2013) e79008.
[5] G. Schlaug, B. Siewert, A. Benfield, R.R. Edelman, S. Warach, Time course of the apparent diffusion coefficient (ADC) abnormality in human stroke, Neurology 49 (1) (1997) 113–119.
[6] T. Warbrick, V. Fegers-Stollenwerk, I.I. Maximov, F. Grinberg, N.J. Shah, Using structural and functional brain imaging to investigate responses to acute thermal pain, J. Pain 17 (2016) 836–844.
[7] J. Rosenberg, I.I. Maximov, M. Reske, F. Grinberg, N.J. Shah, Early to bed, early to rise: diffusion tensor imaging identifies chronotype-specificity, Neuroimage 84 (2014) 428–434.
[8] D.K. Jones, M.A. Horsfield, A. Simmons, Optimal strategies for measuring diffusion in anisotropic systems by magnetic resonance imaging, Magn. Reson. Med. 42 (1999) 515–525.
[9] S. Mori, P. Van Zijl, Diffusion weighting by the trace of the diffusion tensor within a single scan, Magn. Reson. Med. 33 (1) (1995) 41–52.
[10] E.C. Wong, R.W. Cox, A.W. Song, Optimized isotropic diffusion weighting, Magn. Reson. Med. 34 (2) (1995) 139–143.
[11] D. Topgaard, Isotropic diffusion weighting in PGSE NMR: numerical optimization of the q-MAS PGSE sequence, Microporous Mesoporous Mater. 178 (2013) 60–63.
[12] J. Valette, C. Giraudeau, C. Marchadour, B. Djemai, F. Geffroy, M.A. Ghaly, D.L. Bihan, P. Hantraye, V. Lebon, F. Lethimonnier, A new sequence for single-shot diffusion-weighted NMR spectroscopy by the trace of the diffusion tensor, Magn. Reson. Med. 68 (2012) 1705–1712.
[13] S. Eriksson, S. Lasic, D. Topgaard, Isotropic diffusion weighting in PGSE NMR by magic-angle spinning of the q-vector, J. Magn. Reson. 226 (2013) 13–18.
[14] J. Sjölund, F. Szczepankiewicz, M. Nilsson, D. Topgaard, C. Westin, H. Knutsson, Constrained optimization of gradient waveforms for generalized diffusion encoding, J. Magn. Reson. 261 (2015) 157–168.
[15] D. Topgaard, Isotropic diffusion weighting using a triple-stimulated echo pulse sequence with bipolar gradient pulse pairs, Microporous Mesoporous Mater. 205 (2015) 48–51.
[16] S. Eriksson, S. Lasic, M. Nilsson, C.F. Westin, D. Topgaard, NMR diffusion-encoding with axial symmetry and variable anisotropy: distinguishing between prolate and oblate microscopic diffusion tensors with unknown orientation distribution, J. Chem. Phys. 142 (2015) 104201.
[17] C.F. Westin, F. Szczepankiewicz, O. Pasternak, E. Ozarslan, D. Topgaard, H. Knutsson, M. Nilsson, Measurement tensors in diffusion MRI: generalizing the concept of diffusion encoding, Med. Image Comput. Comput. - Assis. Intervent. 17 (2014) 209–216.
[18] F. Szczepankiewicz, S. Lasic, C.F. van Westen, P.C. Sundgren, E. Englund, F. Stahlberg, J. Lätt, D. Topgaard, M. Nilsson, Quantification of microscopic diffusion anisotropy disentangles effects of orientation dispersion from microstructure: applications in healthy volunteers and in brain tumors, Neuroimage 104 (2015) 241–252.
[19] C.F. Westin, H. Knutsson, O. Pasternak, F. Szczepankiewicz, E. Özarslan, D. van Westen, C. Mattisson, M. Bogren, M.J. O'Donnell, M. Kubicki, D. Topgaard, M. Nilsson, Q-space trajectory imaging for multidimensional diffusion MRI of the human brain, Neuroimage 135 (2016) 345–362.
[20] S. Lasic, F. Szczepankiewicz, S. Eriksson, M. Nilsson, D. Topgaard, Microanisotropy imaging: quantification of microscopic diffusion anisotropy and orientational order parameter by diffusion MRI with magic-angle spinning of the q-vector, Front. Phys. (2014) 11.
[21] D. Topgaard, Director orientations in lyotropic liquid crystals: diffusion MRI mapping of the Saupe order tensor, Phys. Chem. Chem. Phys. 18 (12) (2016) 8545–8553.
[22] B. Dhital, E. Kellner, M. Reisert, V.G. Kiselev, Isotropic diffusion weighting provides insight on diffusion compartments in human brain white watter in vivo, Proc. Int. Soc. Magn. Reson. Med. 23 (2015) 2788.
[23] J.P. de Almeida Martins, D. Topgaard, Two-dimensional correlation of isotropic and directional diffusion using NMR, Phys. Rev. Lett. 116 (8) (2016) 087601.
[24] F. Szczepankiewicz, C.F. Westin, F. Stahlberg, J. Lätt, M. Nilsson, Microscopic anisotropy imaging at 7T using asymmetrical gradient waveform encoding, Proc. Int. Soc. Magn. Reson. Med. 24 (2016) 116.
[25] W.S. Price, NMR Studies of Translational Motion: Principles and Applications, Cambridge University Press, 2009.
[26] P.T. Callaghan, Translational Dynamics and Magnetic Resonance: Principles of Pulsed Gradient Spin Echo NMR, Oxford University Press, 2011.
[27] L.L. Latour, K. Svoboda, P.P. Mitra, C.H. Christopher, H. Sotak, Time-dependent diffusion of water in a biological model system, Proc. Natl. Acad. Sci. USA 91 (1994) 1229–1233.
[28] S. Eriksson, S. Lasic, D. Topgaard, Isotropic diffusion weighting in PGSE NMR by magic-angle spinning of the q-vector, J. Magn. Reson. 226 (2013) 13–18.
[29] R. Stirnberg, T. Stöcker, N.J. Shah, A new and versatile gradient encoding scheme for DTI: a direct comparison with the Jones scheme, Proc. Int. Soc. Magn. Reson. Med. 17 (2009) 3574.
[30] J. Andersson, S. Sotiropoulos, An integrated approach to correction for off-resonance effects and subject movement in diffusion MR imaging, Neuroimage 125 (2016) 1063–1078.
[31] A. Leemans, D. Jones, The b-matrix must be rotated when correcting for subject motion in DTI data, Magn. Reson. Med. 62 (2009) 1336–1349.
[32] S. Aja-Fernández, A. Tristán-Vega, S. Hoge, Statistical noise analysis in GRAPPA using a parametrized non-central chi approximation model, Magn. Reson. Med. 65 (2011) 1195–1206.
[33] J. Veraart, E. Fieremans, I. Jelescu, F. Knoll, D.S. Novikov, Gibbs ringing in diffusion MRI, Magn. Reson. Med. 76 (2016) 301–314.
[34] A. Leemans, B. Jeurissen, J. Sijbers, D. Jones, ExploreDTI: a graphical toolbox for processing, analyzing, and visualizing diffusion MR data, Proc. Soc. Magn. Reson. Med. 17 (2009) 3537.
[35] S. Smith, Fast robust automated brain extraction, Human Brain Map. 17 (2002) 143–155.

[36] M. Holz, S.R. Heil, A. Sacco, Temperature-dependent self-diffusion coefficients of water and six selected molecular liquids for calibration in accurate 1H NMR PFG measurements, Phys. Chem. Chem. Phys. 2 (20) (2000) 4740–4742.
[37] E.D. André, F. Grinberg, E. Farrher, I.I. Maximov, N.J. Shah, C. Meyer, M. Jaspar, V. Muto, C. Phillips, E. Balteau, Influence of noise correction on intra- and inter-subject variability of quantitative metrics in diffusion kurtosis imaging, PLoS One 9 (2014) e94531.
[38] I.I. Maximov, H. Thönneßen, K. Konrad, L. Amort, I. Neuner, N.J. Shah, Statistical instability of TBSS analysis based on DTI fitting algorithm, J. Neuroimag. 25 (2015) 883–891.
[39] C. Lebel, C. Beaulieu, Longitudinal development of human brain wiring continues from childhood into adulthood, J. Neurosci. 31 (2011) 10937–10947.
[40] C. Lebel, M. Gee, R. Camicioli, M. Wieler, W. Martin, C. Beaulieu, Diffusion tensor imaging of white matter tract evolution over the lifespan, Neuroimage 60 (2012) 340–352.
[41] I.I. Maximov, F. Grinberg, N.J. Shah, Robust tensor estimation in diffusion tensor imaging, J. Magn. Reson. 213 (2011) 136–144.
[42] C. Lebel, T. Benner, C. Beaulieu, Six is enough? Comparison of diffusion parameters measured using six or more diffusion-encoding gradient directions with deterministic tractography, Magn. Reson. Med. 68 (2012) 474–483.
[43] M.S. Vinding, C. Laustsen, I.I. Maximov, L. Søgaard, J.H. Ardenkjær-Larsen, N.C. Nielsen, Dynamic nuclear polarization and optimal control spatial-selective 13C MRI and MRS, J. Magn. Reson. 227 (2013) 57–61.
[44] L.V. Søgaard, F. Schilling, M.A. Janich, M.I. Menzel, J.H. Ardenkj]aer-Larsen, In vivo measurement of apparent diffusion coefficients of hyperpolarized 13C-labeled metabolites, NMR Biomed. 27 (2014) 561–569.
[45] D. Le Bihan, Apparent diffusion coefficient and beyond: what diffusion MR imaging can tell us about tissue structure, Radiology 268 (2013) 318–322.
[46] J.H. Jensen, J.A. Helpern, A. Ramani, H. Lu, K. Kaczynski, Diffusional kurtosis imaging: the quantification of non-gaussian water diffusion by means of magnetic resonance imaging, Magn. Reson. Med. 53 (6) (2005) 1432–1440.
[47] D.S. Novikov, J.H. Jensen, J.A. Helpern, E. Fieremans, Revealing mesoscopic structural universality with diffusion, Proc. Natl. Acad. Sci. USA 111 (2014) 5088–5093.
[48] M.D. Does, E.C. Parsons, J.C. Gore, Oscillating gradient measurements of water diffusion in normal and globally ischemic rat brain, Magn. Reson. Med. 49 (2003) 206–215.